CHAPTER 1
INTRODUCTION

1.1 Motivation

This study is to observe the flame structure transitions and measure temperature distributions along the vertical centerline of a single Tsuji burner at a fixed cylinder surface fuel-ejection velocity, $V_w = 5$ cm/s, ejected from the forward half part of the burner. Its schematic configuration is given in Fig. 1.1. The varying parameters are the incoming airflow velocity, U_{in}, and the methane to nitrogen ratio, α, in the ejection mixture. For α, the one adopting 99.99% methane (CH_4) as the fuel is served as a reference case. Basically, the present study is an extension and modification of Chang's experiment [1], which used 99.99% methane (CH_4) as the fuel from the Tsuji burner. The spectacular finding in Chang's experimental observation [1] for flame structure was the occurrence of lift-off flame, which later was predicted by numerical simulation of Chen and Tsa [2]. The experimental setup consists of a wind tunnel and a porous sintered cylindrical burner. The wind tunnel is designed to provide a laminar, uniform oxidizer flow over the porous cylindrical burner, from the surface of which the fuel is ejected.   In this work, the major improvement is to employ a gas mixer to generate the assigned mixture of nitrogen and methane and the instrumentation in test section to measure the flame temperature. Those will be described in detail in the following chapter.

By experimental visualization can be observes the whole transition process for flame structures. By comparing the reference one with the ones of different α, we expect to find the flame structure as a function of α under fixed fuel ejection velocity. In addition, by comparison with the corresponding numerical simulations, which are carried out by other study, it can explain the phenomena and causes for the transition of flame structures. These are the main purposes and motivations for this experimental study.

1.2 Literature Review

There are many combustion literatures concerned on counterflow diffusion flame by analytical and experimental studies. In the simulation of counterflow diffusion flame over a single porous cylinder by Chen and Weng [3], they used the two dimensional, complete Navier-Stokes momentum, energy, and species equations with finite-rate chemical kinetics. The main parameters were based on the Damkohler number (Da) and the dimensional fuel-ejection rate ($-f_w$). When Da is decreased, the envelope, side, and wake flames appeared in order. Relatively, decreasing $-f_w$ leads the envelope flame to become a wake flame directly without appearance of side flame. Chen and Tsa [2] modified the original combustion model of Chen and Weng [3], which adopted the four-step chemical kinetics instead of the one–step overall kinetics. The primary parametric study was based on the variations of the incoming airflow velocity and fuel-ejection area, respectively. An existence of lift-off flame is found by their research, whereas it does not exist in Chen's and Weng's study [3].

Chang [1] built a wind tunnel to observe the flame lift-off phenomena over a porous burner and further to explain the flame configurations and transition processes by using a series of photographs. The primary parameters in the experiment were the incoming airflow velocity and fuel ejection velocity, respectively. There were two ejection areas, the half fuel ejection area and the full ejection one, under consideration. For the case of the half fuel ejection area, he found that the stand–off distance decreases and flame length increases with an increase of inflow velocity due to the greater flame stretch effect when fuel ejection rate is fixed. As the increase of inflow velocity, the envelope, wake, side, lift-off and late wake flames appeared in order. However, with a higher fixing fuel ejection rate, the envelope flame directly is transformed into lift-off flame without the appearance of wake flame as inflow velocity increases.

Chen [4] further discussed the relationship between the resultant flames and the corresponding cold flow field without combustion. The smoke-generation technique by using oil spread over a heated wire and the laser-sheet lighting system were used to visualize the cold flow field around porous cylindrical burner in a wind tunnel. She found that in a critical incoming flow velocity, the wake is getting more and more closer to the rear surface of cylinder under a fixed fuel ejection velocity when Re is increased. It might be attributed to the pressure distribution of the flow field. When the static pressure of the downstream wake is greater than the one caused by the blowing over the cylinder surface, the wake is pressed back to the rear of cylinder surface.

Tsuji and Yamaoka [5] studied the laminar counterflow diffusion

3

flame established in the forward stagnation region of a porous cylinder. The flame stability limits and positions as well as the temperature distributions are examined. Two mechanisms for blow-off were identified, namely, the thermal quenching and the flame stretch in flame zone. The critical stagnation velocity gradient is found to depend on the fuel composition, and the fuel composition value can be used as a measure of the over all reaction rate for each combination of reactants. Later, Tsuji and Yamaoka [6] examined the chemical structure and the blow-off mechanism of the laminar counterflow diffusion flame. The concentration distribution of various stable species was measured by a microprobe sampling technique, and the gas-chromatography was used to analyze hydrocarbon flames under various aerodynamic conditions. The overall flame structure was examined by optical interferometer. The flame approaches the cylinder surface when the fuel-ejection rate decreases or stagnation velocity gradient increases. Differences between the concentration profiles in the case of a low fuel-ejection rate and in the case of a large stagnation velocity gradient velocity gradient are significant.

Tsuji and Yamaoka [7] further analyzed the structure of the counterflow diffusion flame, generated in the forward stagnation region of a porous cylinder, and explicated the properties of such diffusion flame. Velocity, temperature, and stable species concentration profiles were measured in detail for methane flames at atmospheric pressure under various aerodynamic conditions. They were determined by two aerodynamic parameters, the non-dimensional fuel-ejection rate, $-f_w$, and the stagnation velocity gradient, $2U_{in}/R$. These distributions were

analyzed to determine the reaction-rate profiles of stable species and the heat-release-rate profiles throughout the flame zone. When $-f_w$ becomes very small, the flame approaches the cylinder surface and both the reaction rates and the heat-release rates decrease considerably, implying that these phenomena might be attributed to thermal quenching of the flame.

In the experiment of Tsuji and Yamaoka [8], they adopted methane-air and methane-hydrogen-air mixtures, which both were diluted with nitrogen, as ejecting fuels to investigate the flame behaviors in the counterflow regions. They found that the concentration percentages of nitrogen influence extinction limits. Over the whole range of equivalence ratio, the maximum allowable nitrogen concentration and extinction limit are slant to the fuel-lean side, where equivalence ratio is less than one.

Tsuji and Ishizuka [9] studied a counterflow diffusion flame established in the forward stagnation region of a porous cylinder. The fuels used were methane and hydrogen, and three inert gases, such as nitrogen, argon, and helium were used as the diluents. As the uniform oxidizer stream velocity was increased or mixture ejection velocity was decreased, the flame approached the cylinder and finally blew off from the forward stagnation region. As the fuel concentration in the ejected mixture or oxygen concentration in the oxidizer stream was decreased, the flame luminosity became weak, and finally the flame blew off.

Dirk et al. [10] utilized Tsuji burner to study the effects of air preheating and simultaneous dilutions of fuel and air stream with nitrogen, argon, and carbon dioxide on the critical strain rate. The air temperature was varied in the wide range from ambient temperature (285 K) to as

high as 1500 K. The critical strain rate, $\dfrac{2V_{air}}{R}\left(1+\dfrac{V_{F,-\infty}}{V_{air,\infty}}\sqrt{\dfrac{\rho_{F,-\infty}}{\rho_{air,\infty}}}\right)$, for

extinction of methane-air diffusion flame in preheated air was measured. When air is diluted to various degrees with argon, carbon dioxide, or nitrogen, the critical strain rates increase exponentially with air temperatures. The obtained critical strain rates from experiments for methane-air diffusion flames in preheated air were reported for air temperature up to 1500 K. Because it was significantly higher than the auto-ignition temperature of stoichiometry methane-air mixture, the extinction occurred for all temperatures.

Jiang et al. [11] used numerical methods to analyze a convective reaction flow over a porous sphere wetted with octane under various flow temperatures, Reynolds numbers, and ambient equivalence rations. In these researches, the porous sphere is initially vaporizing purely. As the flow temperature increases, flame structure first changes to a wake flame, then to a transition flame, and finally to an envelope flame with a premixed reaction zone located close to the nonpremixed flame zone.

Makino et al. [12] experimentally studied the blow-off limits of rich fuel-air flames established in the forward stagnation region of a porous cylinder, from which the premixed methane-air mixture was ejected into a uniform stream. The results showed that the limiting blow-off velocity is increased when the fuel concentration or fuel ejection velocity increase.

Gollahalli et al. [13] presented the results of an experimental program designed to study the wake structures of burning droplets. They adopted pentane as the fuel, ejecting from the porous sphere burner. The droplet was simulated by porous bronze sphere of 6 mm in diameter.

6

They utilized particle track method to study the flow patterns in the flame. The recirculation zone, which exists in the near wake in cold flow, does not exist in the wake and envelope flames. In addition, they found that the envelope flame is transformed into a wake flame at a critical velocity Re = 138.

1.3 Scope of Present Study

The experiments in this study are designed to observe the flame structure transitions and measure the temperature distributions along the vertical centerline of a single Tsuji burner. The main part of experimental apparatus has been set up by Chang [1]. The primary modification is an addition of gas mixing chamber, which can produce the mixture of desired nitrogen-to-methane ratio. The work in the present study can be categorized into two parts, as shown in Fig. 1.2.

In the first part, 99.99% methane (CH_4) is used as fuel, ejected from the forward half area of burner into the incoming airflow. In this part, the varying parameter is the incoming airflow velocity, ranged from 0.41m/sec to 2.63m/sec, under a fixed fuel ejection velocity. It is aimed to visualize the transition process of flame structure behaviors and measure the temperature distribution along the vertical centerline of Tsuji burner.

In the second part, it adopts the mixture, using methane diluted with nitrogen under different percentages, as the fuel. The varying parameters are the methane-to-nitrogen ratio in the ejection mixture and the incoming airflow velocity. In the experimental investigation, the flame configurations are photographed by a digital video in the whole process and the vertical centerline flame temperature distributions are measured

by using R-type thermocouples. The purpose of this experiment is to investigate the relationship between the methane-to-nitrogen ratio and the vertical centerline flame temperature distributions that can further to explain clearly the cause for the transition of flame structures. Furthermore, the results obtained from this experiment are compared with the corresponding predications by Chen's numerical simulation [14] to confirm the experimental credibility.

CHAPTER 2
EXPERIMENTAL APPARATUS

In this present study, the experimental apparatuses basically are same as these in Chang's equipments [1], except that temperature measurement instrumentation in the test section and a gas mixer to generate the mixture of desired methane-to-nitrogen ratio are added. The apparatus consists of four major elements, which are the wind tunnel, gas mixer, Tsuji burner and measurement instrumentations. The schematic configuration is shown in Fig. 2.1. The above-mentioned elements are described in details as follows.

2.1 Wind Tunnel

A wind tunnel is designed to be able to provide a laminar, uniform oxidizer flow to the porous burner. It is open-circuit and oriented vertically upwards. The tunnel comprises five parts, which are the blower, diffuser, flow straightener, contraction and test section. The design concepts about the wind tunnel are mainly from a NIST paper [16], and also comply with the standard of AMCA210-85 [17]. The schematic configurations are shown in Fig. 2.2 and Fig. 2.3.

2.1.1 Blower

The airflow in the tunnel is supplied by a variable-frequency blower, in which frequency is directly converted into desired velocity by converter. The correlation between the blower frequency and resultant velocity in test section is demonstrated in Fig. 2.4. It is obtained by the

measurements of pitot tube.   Also, the correlation measured by hot wire is compared with Chang [1] and Chen [18].   It reveals that both are quite similar, but the velocities measured by the hot wire are slightly higher when the frequency is less than 11 Hz.   In order to avoid the influence of vibration, the bases of wind tunnel and blower are separated (see Fig. 2.5).

2.1.2 Diffuser

A 30 cm long diffuser has an inlet cross-section area of 12x12 cm^2 and the outlet one is 40x40 cm^2.   The expansion ratio based on area is 1:11.

2.1.3 Flow Straightener

The airflow from the diffuser section is unstable before entering into the follower contraction section.   A flow straightener is used to make it more stable.   The flow straightener section, which serves to insure that the flow to test section is laminar and uniform over the entire cross-section, is made of honeycomb and screen.   The screen is mounted to decrease disturbances to make flow uniform.   The honeycomb is added to the utilities of screen to reduce flow turbulence further.   With appropriate combination of screen and honeycomb and putting them at optimum position, it can achieve the goals mentioned above.

2.1.4 Contraction Section

The purpose of contraction section is to provide a uniform flow field into the test section. The design standards intend to shorten the duct and reduce boundary layer thickness along the wall as possible.

2.1.5.1 Test Section

The test section has a cross section area of 24x4 cm^2 and a length of

30 cm. It is made up of four sides. In the front and two adjacent sides, they are equipped with quartz-glass plates as the observation windows. The quartz-glass plates can sustain a high temperature up to 1,500°C. The downstream of test section is connected to a diffuser (500 mm), which can reduce the velocity of exhaust gases from test section. The vent follows after the diffuser to outdoor. The rear part of the vent can resist high temperature by adhering fins onto the inside of vent as heat exchanger. The outside of vent is equipped with a water-cooling system, including cooler, water tank and pump, as shown in Fig. 2.6. The uniformity and stability of flow velocity in test section is confirmed by following procedure. There are four pitot tubes and a fixed static pressure hole in the front of the burner of the test section (as shown in Fig. 2.7). Change different connection in order for the four pitot tubes with the fixed static pressure hole under the same inflow velocity after a long time. If the pressure difference is closely equal, then we can certain that the flow is uniform and stable ahead of the burners, see Fig. 2.8 for the demonstration.

2.1.5.2 Temperature measurement in test section

The rear side of the test section is modified to allow probe inserting into the flame properly to measure the temperatures along the vertical centerline. Nine R-type thermocouples are used to measure flame temperatures, two of them are located in the front of the cylinder burner and the others are behind the burner. The two measuring positions in the front of the cylinder burner are located at the distances of 2.5 mm and 5 mm ahead of the forward burner surface as shown in Fig. 2.9. The other seven positions as shown in Fig. 2.10 are 2.5-, 5-, 7.5-, 15-, 30-, 45- and

60-mm downstream of the cylinder surface. The diameter of holes is 1.7 mm. When the thermocouple is inserted into the hole to measure the temperature, the gap between the hole and probe is filled with noncombustible material to prevent the gas from leakage.

2.2 Porous Sintered Cylindrical Burner

2.2.1 Burner Structure

For this experimental requirement, the design of burner must be able to endure the high temperature. The burner consists of the inner and outer parts, respectively. The outer part is the replaceable sintered stainless steel, which is $20\,\mu\text{m}$ pores and has a length of 40 ± 0.5 mm. Its inner diameter is 20 ± 0.5mm, and the outer one is 30 ± 0.5 mm as shown in Figs. 2.11 and 2.12. The advantage of such design is that the burner replacement can be easily performed whenever clogging or damage on the porous burner surface occurs owning to long time burning. In the inner part, it is a cylindrical brass rod (see Fig. 2.13) with an internal water-cooling groove and fuel supply groove. The outer part is screwed onto the inner part. The cooling water through groove is used to reduce the surface temperature of burner and prevent it from damages.

2.2.2 Burners Equipped to test section

The present study uses a single burner, whose rear half surface is coated with several temperature-resistant layers to prevent the fuel ejection into the wake region. The fuel ejection is from front half fuel-ejection surface of the burner in the present experiment. The fuel used is the 99.99% methane (CH_4) and different concentrations for

methane diluted with nitrogen by gas mixer, the fuel flow rate is controlled and measured by a digital flow meter with a microprocessor of high capability inside.   The fuel flow rate and control signal are digitized by a 16-bit A/D converter in the CPU, and then they are transformed into analog ones by the same converter.   The fuel ejection velocity is calculated by dividing the fuel volumetric flow by the available fuel ejection area along burner surface.

2.3 gas mixer

The gas mixer system consists of spiral mix tube, check valve, mass flow controller, pressure gauge, power supply and control unit, which is shown in Fig. 2.14 and Fig. 2.15. The schematic configuration of gas mixer is shown in Fig. 2.16. Methane and nitrogen are supplied from the respective gas cylinders, whose outlet pressures are controlled and fixed at 1kg/cm^2 by using pressure regulator.   These two gases respectively pass through the inlet ports of mixer, equipped with the pressure gauge, mass flow controller and check valve.   Then, methane and nitrogen with the desired volume flow rates controlled by mass flow controllers enter the spiral tube to mix each other in the mixer. Finally the mixture gas passes through the outlet pressure gauge and mass flow controller at the desired volume flow rate. The gas mixer function is to well mix the methane with nitrogen in an assigned fraction. The interesting parameter is mass fraction rather than volume fraction. Therefore, the transformation between mass and volume fractions is described as follow.

$$Y_{CH_4} = \frac{X_{CH_4} \times M_{CH_4}}{X_{CH_4} \times M_{CH_4} + X_{N_2} \times M_{N_2}}$$

$$= \frac{X_{CH_4} \times M_{CH_4}}{X_{CH_4} \times M_{CH_4} + \left(1 - X_{CH_4}\right) \times M_{N_2}}$$

$$= \frac{16.04 \times X_{CH_4}}{28.016 - 11.976 X_{CH_4}}$$

Therefore,

$$X_{CH_4} = \frac{Y_{CH_4} \times 28.016}{16.04 + Y_{CH_4} \times 11.976}$$

where Y_{CH_4} and X_{CH_4} represent the mass fraction and volume fraction respectively.

2.4 Measurement Instrumentations

2.4.1 R-type thermocouple

The flame temperatures near the burner are measured by a 0.35mm diameter R-typed bare wire thermocouple as shown in Fig. 2.17. Thermocouple junctions are formed by butting Pt and Pt 10%Rh wires together and flame welding. The signals from the thermocouple are sent to a PC-record (RS-232).

2.4.2 Nozzle of Standard of AMCA 210-85

The measurement of inlet velocity at the test section adopts the AMCA 210-85 standard of nozzle-method to measure the volume flow rate and then to deduce the flow velocity. The standard is used to establish uniform flows for laboratory testing of fans and other air moving devices by AMCA. There are three nozzles (ϕ:10, 15, 30 mm)

and four sets of pitot tubes distributed evenly inside the cylinder (see Fig. 2.3). They are used to measure the local velocities inside the cylinder. Then it can get total volume flow rate to deduce velocity of test section by dividing cross section area in test section.   The accuracy, described by AMCA 210-85, is within 3 % when velocities are ranged from 0.21 m/s to 3.3 m/s, and it becomes 5 % as the velocity is smaller than 0.21 m/s.

2.4.3 Digital Video

The visualization of flame is assisted by a digital video (Type DCR-TRV40, SONY), which is fixed at an appropriate position to monitor flame variations. The images from the video are transmitted to a PC by IEEE 1394 card, and the images are processed by Adobe Premiere 6.0 software to show flame behaviors in different incoming flow velocity and concentration of methane with nitrogen.

2.4.4 Spotlight software

In this present study, it uses Spotlight 1.0 software to analyze blue color pixel in the flame pictures that can define envelope flame thickness, stand off distance and attached angle, as shown in Fig. 2.18. The width of one pixel is found by the following way.   The diameter of cylinder burner is 30mm, which is equal to 75 pixels shown in the picture, so one pixel of the picture is equivalent to a real distance of 0.4 mm approximately.   (Spotlight   1.0,   developed   by   NASA (**http://microgravity.grc.nasa.gov/spotlight/**),   is   a   cross-platform GUI-based software package designed to perform image analysis on sequences of images.) Those definitions mentioned above will be used to characterize the respective flame behaviors.

2.5 Procedure of the Experimental Operation

(1) Calibrate the instruments to insure the stabilization and accuracy of their performance before performing the experiment.

(2) Warm up the apparatuses, such as blower and mass flow controller.

(3) The blower has to be operated for 30 minutes in advance until the flow uniformity and stabilization are achieved.

(4) Check if any fuel gases leakage from pipelines by applying suds on them.   It is very important procedure especially for the use of the achromatic, flavorless, toxic and flammable fuel.

(5) Turn on the gas mixer and set the fuel flow rate to the desired methane to nitrogen ratio.

(6) Open the valve of methane fuel cylinder and nitrogen cylinder retain the inlet pressure up to 0.55kg/cm^2, and then turn on the stop valve of mass flow controller.   When the alarm light of mass flow controller displays green, it indicates that the fuel passes pipelines to burner.

(7) Turn on the cooling systems of the burner and vent.

(8) Turn on the ignition device, a spark produced by 3000 volt high voltage, to initiate a flame.   Turn it off as the flame is established.   Note that it should start the ignition before turning on the fuel supply valve; otherwise it may cause an explosion.

(9) At first part of present study, observe the flame structure variations by changing the inflow velocities from a lower one to

higher one under a fixed fuel ejection velocity. In the second part, firstly vary methane to nitrogen ratio and certain fixed value of fuel ejection velocity, and then changing the inflow velocities from a lower to higher.

(10) Set the digital camera in a fixed position to get the same observation view of test section to catch all images from the flames.

(11) For the second part, change the different ratio of methane to nitrogen. Repeat the procedure from (8)-(10) steps.

(13) Replace the rear side of test section to let the R-type thermocouple insert into the test section to measure the flame temperatures in the arrangement of the circular apertures. Repeat the procedure from (8)-(10) steps.
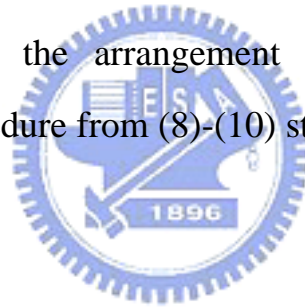
CHAPTER 3
UNCERTAINTY ANALYSIS

The accuracy of the data from experimental results should be confirmed before the analyses of experimental results are carried out since the data may not be equally good to adopt. Uncertainty analysis (or error analysis) is a procedure used to quantify data validity and accuracy [19]. Experimental measuring results in errors. Experimental errors can be classified into the fixed (systematic) error and random (non-repeatability) error, respectively [18]. And fixed error is the same for each reading and can be removed by proper calibration and correction. Oppositely, random one is different for every reading and hence cannot be removed. The purpose of uncertainty analysis is to estimate the probable random error in experimental results.

From the viewpoint of reliable estimation, it can be categorized into single-sample and multi-sample experiments. If experiments could be repeated enough times by enough observers and diverse instruments, then the reliability of the results could be assured by the use of statistics [19]. Like such, repetitive experiments would be called multi-sample ones. Experiments of the type, in which uncertainties are not found by repetition because of time and costs, would be called single-sample experiments.

3.1 Analyses of the Propagation of Uncertainty in Calculations

Uncertainty analysis is carried out here to estimate the uncertainty levels in the experiment. Formulas for evaluating the uncertainty levels in the experiment can be found in many papers [19,20] and textbooks [18,21,22]. They are presented as follows:

Suppose that there are n independent variables, $x_1, x_2, \ldots, x_n$, of experimental measurements, and the relative uncertainty of each independently measured quantity is estimated as u_i. The measurements are used to calculate some experimental result, R, which is a function of independent variables, $x_1, x_2, \ldots, x_n$; $R = R(x_1, x_2, \ldots, x_n)$.

An individual x_i, which affects error of R, can be estimated by the deviation of a function. A variation, δx_i, in x_i would cause R to vary according to

$$\delta R_i = \frac{\partial R}{\partial x_i} \delta x_i .$$
(3-1)

Normalize above equation by dividing R to obtain

$$\frac{\delta R_i}{R} = \frac{1}{R} \frac{\partial R}{\partial x_i} \delta x_i = \frac{x_i}{R} \frac{\partial R}{\partial x_i} \frac{\delta x_i}{x_i}$$
(3-2)

Eq. (3-2) can be used to estimate the uncertainty interval in the result due to the variation in x_i. Substitute the uncertainty interval for x_i,

$$u_{R_i} = \frac{x_i}{R} \frac{\partial R}{\partial x_i} u_{x_i}$$
(3-3)

To estimate the uncertainty in R due to the combined effects of uncertainty intervals in all the x_i's, it can be shown that the best representation for the uncertainty interval of the result is [20]

$$u_R = \pm \left[\left(\frac{x_1}{R} \frac{\partial R}{\partial x_1} u_1 \right)^2 + \left(\frac{x_2}{R} \frac{\partial R}{\partial x_2} u_2 \right)^2 + \ldots + \left(\frac{x_n}{R} \frac{\partial R}{\partial x_n} u_n \right)^2 \right]^{1/2}$$
(3-4)

3.2 Uncertainty Level Analysis in the Experiment

The results of all uncertainty analyses according to the calculations of above formula are summarized in Table 3.1. Several parameters are selected to demonstrate the process of uncertainty level analyses as follows.

The cross-section area of test section, A, is

$A = a \times b$, $a = 240 \pm 0.5mm$, $b = 40 \pm 0.5mm$

$A = A(a,b)$

$u_a = \dfrac{0.5}{240} = 0.00208$, $u_b = \dfrac{0.5}{40} = 0.0125$

$u_A = \pm \left[\left(\dfrac{a}{A} \dfrac{\partial A}{\partial a} u_a \right)^2 + \left(\dfrac{b}{A} \dfrac{\partial A}{\partial b} u_b \right)^2 \right]^{1/2} = \pm \left[(u_a)^2 + (u_b)^2 \right]^{1/2} = \pm 0.01267$

The surface area of burner, A_{Burner}, is

$A_{Burner} = \pi D L_B$, $D = 30 \pm 0.5mm$, $L_B = 40 \pm 0.5mm$

$A_{Burner} = A_{Burner}(D, L_B)$

$u_{A_B} = \pm \left[\left(\dfrac{D}{A_B} \dfrac{\partial A_B}{\partial D} u_D \right)^2 + \left(\dfrac{L_B}{A_B} \dfrac{\partial A_B}{\partial L_B} u_{L_B} \right)^2 \right]^{1/2}$

($u_D = \dfrac{0.5}{30} = 0.01667$, $u_{L_B} = \dfrac{0.5}{40} = 0.0125$)

The uncertainty of airflow velocity:

$U_{in} = \dfrac{\dot{V_0}}{A}$, U_{in}: Airflow velocity, $\dot{V_0}$: Flux of air

$u_{U_{in}} = \pm \left[\left(u_{\dot{V_0}} \right)^2 + \left(-u_A \right)^2 \right]^{1/2}$

The uncertainty of fuel-ejection velocity:

$V_w = \dfrac{Q_{fuel}}{A_{Burner}}$, V_w: Fuel velocity, Q_{fuel}: Flux of fuel

$$V_w = V_w\left(Q_{fuel}, A_{Burner}\right)$$

$$u_{V_w} = \pm\left[\left(u_{Q_{fuel}}\right)^2 + \left(-u_{A_{Burner}}\right)^2\right]^{\frac{1}{2}}$$

The uncertainty of Reynolds number, u_{R_e} is

$$R_e = \frac{U_{in}R}{\nu},$$

$$u_{R_e} = \pm\left[\left(u_{U_{in}}\right)^2 + \left(u_R\right)^2 + \left(-u_\nu\right)^2\right]^{\frac{1}{2}}$$

The uncertainties of the properties are

$$u_{\rho(T)} = \pm\frac{\delta\rho}{\rho} = \frac{1}{\rho}\frac{d\rho}{dT}\left(\pm\delta T\right)$$

$$u_{\nu(T)} = \pm\frac{\delta\nu}{\nu} = \frac{1}{\nu}\frac{d\nu}{dT}\left(\pm\delta T\right)$$

The uncertainty of P_{sat} is

$$ln(P_{sat}(T_0)) = 23.2 - \frac{3816}{(-46+T_0)}$$

$$P_{sat} = e^{23.2-\frac{3816}{(-46+T_0)}}$$

$$u_{P_{sat}} = \frac{T}{P_{sat}}\frac{\partial P_{sat}}{\partial T}\frac{\partial T}{T}$$

3.3 The Asymmetric Uncertainties of Thermocouple for Flame

Temperatures of the flame over a burner are measured by a 0.35mm diameter R-typed bare wire thermocouple. The signals from the thermocouple are sent to a PC-record (RS-232). The accuracy of the thermocouple itself without coating T_t is $\pm0.2\%$. It is worthwhile to check the correctness of gas temperature measured by such R-typed thermocouple through the effects of conduction, convection, and radiation.

According to the balance of energy, namely,

Energy in = Energy out, or

Convection to the junction of thermocouple = Radiation from the junction of thermocouple + Conduction loss from the probe

The conduction term mentioned above can be neglected because the wire of thermocouple is fine (0.35mm). Then, the steady-state energy equation can be rewritten as follows [23].

$$\frac{4h}{D_w}(T_g - T_t) - \frac{4\sigma}{D_w}(\varepsilon T_t^4 - \varphi T_w^4) = 0 \qquad (3\text{-}5)$$

Relative to the high flame temperature, usually above $1000^\circ C$, the wall temperature is low enough to remove the absorption term, φT_w^4, from Eq. (3-5).

So, the expression of correlation is given as:

$$T_g = T_t + \frac{\varepsilon \sigma T_t^4}{h} \qquad (3\text{-}6)$$

where T_g = the true gas temperature

   ε = emissivity of the thermocouple

   σ = Stefan Boltzmann constant

   h = convection heat transfer coefficient at thermocouple wire surface

The expressions of h and ε are mentioned in this paper [23]. Now, the analysis method of uncertainty can be utilized to obtain the uncertainty in the flame temperature from the correlation associated with h, T_t and ε. Via the uncertainty calculation, it finds the maximum uncertainty value to be 112 K when the gas temperature along the centerline is up to 1390 K. On the other hand, it has the minimum

uncertainty value as 0.38 K when the gas temperature is 298 K. Consequently, the percentage of uncertainty value is varied from 0.12 % to 8.1 % as the corresponding value is changed from 0.38 K to 112 K.

3.4 Effect of Preheated in the Test Section

Performing this experiment, it is found that the flame transition limits would be larger if the measurements are not taken until the front and back walls of the test section are cooled down completely. The discrepancy might be up to 0.3 m/s. Besides, between 6~18 seconds after ignition, the discrepancy is found to be about 0.2 m/s per 6 seconds. This is because that the incoming flow has been preheated in advance. As a consequence, the flame transitions will be delayed. This phenomenon was explained by Jiang et al. [11]. Although, this experiment measures the corresponding flame transition limits individually, the transient time to the desired incoming velocity after ignition will take approximately 6~9 seconds to reach stable condition. Hence, the preheated effect can not be avoided.

3.5 The Experimental Repeatability

In order to confirm the accuracy and confidence of the experiment, the procedures of changing the airflow velocities for each methane to nitrogen ratio α were executed three times to ensure the experimental repeatability. The transition velocity is a critical value to investigate the flame behaviors as the increasing incoming velocity. Flame transformation ahead of the half fuel-ejection area is a function of methane to nitrogen ratio. It recorded three measured data and made an averaged value for each α. The averaged values formed an

approximate curve. The three measured data, their corresponding averaged value and the error are listed in Tables 3.2 and 3.3 for the envelope flame transition and wake flame transition velocities, respectively. The error is defined as the ratio of the absolute difference value between the maximum and minimum values among the three data to their averaged value, the error bar is approximately $\pm$ 0.02m/sec. It can be seen that the errors are within the acceptable range (the maximal one is under 5.71%) in general and the repeatability is moderately excellent. Fig. 3.1 graphically exhibits the presentations of Tables 3.2 and 3.3. In terms of flame transition processes, it will be discussed in detail in next chapter.

CHAPTER 4
RESULTS AND DISCUSSION

The experimental work mainly investigates the flame transition processes as the functions of nitrogen mass concentration in the gaseous fuel and incoming velocity over a single Tsuji burner. The ejection velocity of methane/nitrogen mixture from the forward half surface of burner is fixed at ejection 0.05 m/s. However, the actual experimental process is that it fixes the assigned composition of fuel firstly, then, changes the incoming velocity, from 0.41 to 2.63 m/sec, to observe the corresponding flame configuration. The same procedure is carried out again when another fuel composition is taken into consideration. Except the flame configuration observation, the temperatures along the symmetrical line of the cylindrical burner are also measured.

4.1 Flame Transition Processes

The flame configuration map is shown in Figure 4.1. The ordinate is the incoming velocity, whereas the abscissa is the mass fraction of methane in the methane/nitrogen fuel mixture (α). The latter definition can be referred in Chapter 2.3, and it is rewritten as follows.

$$Y_{CH_4} = \frac{X_{CH_4} \times M_{CH_4}}{X_{CH_4} \times M_{CH_4} + X_{N_2} \times M_{N_2}} = \frac{X_{CH_4} \times M_{CH_4}}{X_{CH_4} \times M_{CH_4} + \left(1 - X_{CH_4}\right) \times M_{N_2}}$$

$$= \frac{16.04 \times X_{CH_4}}{28.016 - 11.976 X_{CH_4}} = \alpha$$

Note that it reassigns Y_{CH_4} as α here. The incoming velocities used in

the experimental observation of flames for each α are listed in Table 4.1. In this table, the data of demarcation lines shown in Fig. 4.1 are also included, and they are circle-marked.

It can be seen that in the higher methane mass fraction regime, ($\alpha > 60\%$), the envelop, transition and wake flames appear in order as the incoming flow velocity increases from 0.41 to 2.63 m/sec. A transition zone between envelop and wake flame regions is identified in this regime. In such zone, the flame shows an oscillatory feature. It is highly unstable such that it might appear as a lift-off flame, wake flame or extinction. The detailed description will be given latter. On the other hand, when the methane to nitrogen mass ratio is below 60% ($\alpha \le 60\%$), the envelope flame is directly transformed into wake one as incoming velocity gradually increases up to the transition velocity, and no transition flame is identified in this regime.

The following two sections are used to further demonstrate the flame configurations and behaviors shown in Fig. 4.1.

4.2 Case of pure methane as the fuel

At the beginning, the case to be discussed is that the composition of fuel used is pure methane, or $\alpha = 100\%$ in Fig. 4.1. The variations of flame configuration as a function of incoming flow velocity are shown in Fig. 4.2. It can be seen that, the envelope flames, transition region, and wake flames appear in order when inflow velocity increases. These flames are discussed in details as follows.

4.2.1 Envelope Diffusion Flame

The envelope flames surrounding the porous cylinder and spreading

to downstream in the low-speed flow regime, from 0.41 to 1.24 m/sec, are shown in Figs. 4.2(a) and 4.2(b).

The definitions of stand-off distance and flame thickness in the forward stagnation region for envelope flame are graphically illustrated in Fig. 2.18. Tables 4.2 and 4.3 list the values of flame thickness and stand-off distance. It can be seen that both of them are decreased as incoming airflow velocity increases. An increase of incoming flow velocity represents an increase in flame stretch so that the flame thickness becomes thinner. In the meantime, the convection of air flow becomes stronger to push flame front toward the burner surface. For this case, the maximum flame thickness and stand-off distance are 2.4 mm and 1.7 mm, whereas the minimum ones are 1.3 mm and 1 mm, respectively, occurred in the neighborhood of transition velocity (U_{in} = 1.24 m/s). Both minimum values can be regarded as the critical ones, behind which no flame front can be sustained ahead of the cylindrical burner. However, from these tables, the changes of the flame thickness and stand-off distance with the incoming velocity are step-wise rather than continuous. It is attributed to the insufficiency in pixel and resolution of experimental photographs. Remind that one pixel width is 0.4 mm approximately as mentioned in Chapter 2.4.3. Therefore, the errors for these two values are expected relatively large.

Figure 4.3 shows the two measured temperatures ahead of the burner as a function of incoming velocity. Their positions are 2.5 mm and 5.0 mm in front of the burner forward surface as shown in Fig. 2.9. From this figure, it can show that the flame is moving toward the burner surface as the incoming flow velocity increases. Also, in the flow velocity

range, 0.41~1.00 m/s, the thermocouple at 2.5mm location is inside the flame zone according to the data of flame thickness and stand-off distance in Table 4.2 and 4.3.   The one of U_{in} =0.51 m/s is almost at the middle of the flame zone, therefore, it can catches the maximum flame temperature, 1098K.   As U_{in} greater than 1.00 m/s, the thermocouple at 2.5mm location is out of the flame zone, so its temperature shows a drop. For an example, it is 657 K as U_{in} = 1.09 m/s comparing to 882K as U_{in} = 1.00 m/s. When it approaches the transitional velocity (U_{in}= 1.24 m/s), the temperature is lowered to 487 K.   As for the thermocouple at the 5 mm ahead of the cylinder surface, it is always outside the flame zone from the values given by Table 4.2 and 4.3.   Therefore, it shows an asymptotic decreasing trend as the flame is shifting toward the burner surface due to the increase of incoming flow velocity.

Figure 4.4 shows the seven temperature measurements downstream of the burner as a function incoming flow velocity.   The measuring positions are 2.5, 5, 7.5, 15, 30, 45 and 60 mm behind the burner rear surface, respectively; see Fig. 2.10.   It can be seen that in this range the combustion plumes, where the active reactions are still maintained, on the two sides of cylinder are shifted inward toward the center line due to their interactions with the outer convective flow.   Since the centerline theoretically is a symmetrical line, it behaves like an adiabatic boundary. Therefore, the temperatures from x= 2.5 to 60 mm along the center line are increased as long as it is an envelop flame.   Also, the temperature at the same position increases as the flow velocity increases.   It is because that the larger velocity provides a greater shear force at the interface between the flame and air flow that pushes the flame inward more.

4.2.2 Transition Flame

When the inflow velocity increases up to 1.26 m/sec, the flame front is broken suddenly and is retreated to far downstream of the rear surface of the cylindrical burner. It is defined as flame transition region (see Fig. 4.1), whose flame configurations are shown in Figs. 4.2(c) and 4.2(d). In this region, the lift-off flame front in the range of U_{in} between 1.24 to 1.53 m/ sec oscillates back-and-forth without a specified frequency because the balance position changes all the time and it can only survive for 5 to 8 seconds. These behaviors are shown in Fig. 4.5, which is made up 9 pictures at different time under the fixed incoming airflow velocity 1.26 m/s. It is found that the flame behind the cylinder lacks a recirculating flow to stabilize it that might be the reason why the flame is unable to stay behind the cylinder. So, we call the flames in this range are in a transition process.

4.2.3 Wake Flame

When the inflow velocity exceeds 1.56 m/sec, the flame front retreats along the cylinder surface, then the flame front can stabilize on the rear part of the cylinder as shown in Figs. 4.2(e) and 4.2(f). Its existing range is from U_{in} = 1.56 to 2.63 m/s. The ejecting fuel from the forward burner surface is mixed with the incoming oxidizer to make up a flammable mixture, which is carried to downstream and subsequently ignited by the recirculated hot gas behind the cylinder to initiate the reaction to form the wake flame.

The definition of attached angle for wake flame is shown in Fig. 2.18. At U_{in}= 1.56 m/s, the wake flame transition limit velocity, its attached

angle is 154°. As incoming airflow velocity increases, the flame attached angle is decreased as shown in Table 4.4. An increase in incoming airflow velocity intensifies the stretch and convection that let the flame front shift inward and downstream.   However, more fuels are carried downstream and the mixing with air is better by the faster incoming flow that makes the wake flame front become stronger.   Apparently, the latter effect outweighs the former one, so the flame front moves forward along the burner surface to cause a smaller attached angle.

Figure 4.6 shows the flame temperature along the vertical centerline behind the burner. It can be seen that in the range of U_{in} = 1.56 to 2.06 m/s, two combustion plumes following their respective flame fronts exist on the two sides of rearward cylinder (Figs. 4.2(e) and 4.2(f)).   The combustion plumes are shifted inward due to the shear by the outer air flow.   Eventually, two plumes are merged on the centerline.   Therefore, the temperatures from x= 2.5 to 45 mm along the center line initially are increased. Up to 60mm, it is found that its temperature is lower than that at 45 mm.   Apparently, the combustion plumes end between 45 and 60mm, and then they become thermal plume.   For example, T = 1240K at 60mm of measuring position comparing to T=1317K at 45mm when U_{in} = 1.77 m/s. The temperature increases as the inflow velocity increases at the same position, the reason is similar to that occurred in envelop flame, mentioned above.

Comparing to temperature variation in the range of U_{in}=1.56 to 2.06, the temperatures at 2.5, 5, 7.5, 15, 30 and 45mm increase very slightly as inflow velocity increases between U_{in} = 2.06 to 2.63 m/s. However, the ones at 60mm increase sharply in that range.   Especially at U_{in} = 2.63

m/s, the maximum inflow velocity can be reached at the present experiment, the temperature at 60mm of measuring position is higher that measured 45mm, indicating that the combustion flume is stretched to become longer in that inflow range.

4.3 Case of methane/nitrogen fuel mixture

After complete the above experimental study for pure methane case, the following parametric studies are based on the variation of methane-to-nitrogen mass ratio in the fuel mixture, which α varies from 90% to 40%. For each α, the incoming airflow velocities changes from 0.41 to 2.63 m/s as well. It is intended to find the relations between the mass fraction of methane in the fuel mixture (α) and inflow velocity (U_{in}) for flame transition behaviors. The complete flame configuration map iss shown in Fig. 4.1, which can be divided into two regimes. In the lower methane mass fraction regime, ($\alpha \leq 60\%$), the envelop flame directly transforms into wake flame, whereas in the higher methane mass fraction regime, ($\alpha > 60\%$), there exists a transition zone between envelop and wake flames. Two cases, $\alpha = 60\%$ and $\alpha = 80\%$, are selected to demonstrate their features.

4.3.1 $\alpha = 80\%$

4.3.1.1 Envelope Diffusion Flame

The envelop flame characteristics is similar to $\alpha = 100\%$. In this case, the maximum flame thickness and stand-off distance are 2 mm and 1.7 mm occurred at 0.41 m/s of incoming airflow velocity, whereas the minimum ones are 1.3 mm and 1 mm, respectively at the neighborhood of

transition velocity (U_{in} = 1.14 m/s), as shown in Table 4.2 and 4.3. The corresponding envelope flame photographs for α = 80% are shown in Fig 4.7(a) and 4.7(b). Comparison with α=100%, the difference in maximum flame thickness is 0.4mm at the same incoming airflow velocity 0.41 m/s. It is because the flame becomes weaker when the methane mass ratio is lowered so that the envelop flame front becomes thinner. However, the flame thicknesses at the respective transition velocities, U_{in}= 1.24m/s and 1.14 m/s, for both α=100% and α=80% are the same; 1.3mm. The possible reason is that the flame stretch effect approaches the limit at the transition velocity.

Comparing the stand-off distance with α=100%, it finds that the stand-off distance strongly depends on the incoming airflow velocity, but not on the methane to nitrogen mass ratio. It is because that the stand-off distance, or quench distance, is decided by the velocity gradient at the wall and the wall temperature.

Figure 4.8 shows the two measured temperatures ahead of the burner as a function of incoming velocity. Comparing α=100% (Fig.4.3) with the present case, the temperatures are 1,098 K and 916 K, respectively, at 2.5mm location under U_{in} =0.51 m/s, because the thermocouple is at the outside of flame zone for α=80% according to Table 4.2 and 4.3. For other incoming airflow velocities, the trend is the same. So does the thermocouple at 5mm upstream of the burner.

Figure 4.9 shows the seven temperature measurements downstream of the burner as a function incoming flow velocity. It shows that the variation trend for α=80% is the same as that in α=100%, only with the lower corresponding temperatures. These temperature measurements

indicate that the flame become weaker as methane to nitrogen mass ratio decreases.

4.3.1.2 Flame Transition

At $\alpha=80\%$, the transition velocity that the envelope flame is transformed into a transition flame, is 1.16 m/s, which is lower than 1.26 m/s of $\alpha=100\%$. Of course, it also indicates that the flame at $\alpha=80\%$ is weaker. Therefore, the envelope flame is more easily to blown off comparing to that of $\alpha=100\%$.

As methane to nitrogen mass ratio is below 60%, the envelope flame will transform into wake one directly without any appearance of transition flame when incoming velocity gradually increases to a limiting value, therefore the limit of flame transition behaviors exists between $\alpha=60\%$ and $\alpha=70\%$.

Figure 4.10 shows the transition flame configuration at $U_{in} = 1.24$m/s. The behaviors are similar to those described in Fig. 4.5.

4.3.1.3 Wake Flame

When the inflow velocity exceeds 1.46 m/sec, the flame front can stabilize on the rear surface of the cylinder as shown in Figs. 4.7(e) and 4.7(f). At $U_{in}= 1.46$ m/s, the wake flame transition limit velocity, its attached angle is 149° (see Table 4.4). Comparing the variation of attached angle as a function of incoming flow velocity with $\alpha=100\%$, the trend is similar. However, the angle may not always be larger for the case with higher α under the same U_{in}. For example, the attach angle is 143° for $\alpha=70\%$, whereas it is 141° for $\alpha=90\%$ and 80% under $U_{in} = 1.58$ m/s. However, the discrepancy is quite small that the measurement error may

take the responsibility.   Finally, it is found that the variation of attached angle change is not so obvious at the present cylinder burner with 30mm-diameter under different methane to nitrogen ratios.

Figure 4.11 shows the temperature distributions at the seven measuring positions in the rear of the cylinder burner for wake flame. Totally speaking, the temperatures for $\alpha=100\%$ are slightly higher than those in the present case.   It is because the flame is weaker for $\alpha=80\%$. At $U_{in} = 1.46$ to 2.06 m/s, the variation trend of temperature generally is similar to that $\alpha=100\%$ (Fig. 4.6), but with few exceptions.   The temperatures at 45mm and 60mm of measuring positions are found lower than the one at 30 mm.   The reason is that the combustion plume becomes is shortened as methane to nitrogen ratio decreases.   As U_{in} is greater than 2.06 m/s, the temperature varying trend is still generally similar to that of $\alpha=100\%$, except those at the 15mm, 35mm, 45mm and 60mm of the measuring position at $U_{in} = 2.25$m/s.   It is found that the temperatures at these points are decreased rather than increased as inflow velocity exceeds 2.25m/s.   It is also because the combustion plume becomes smaller comparing to that of $\alpha=100\%$.

4.3.2 α = 60%

4.3.2.1 Envelope Diffusion Flame

The corresponding photographs for $\alpha = 60\%$ are shown in Fig 4.12(a) and 4.12(b). In this case, the maximum flame thickness and stand-off distance are 1.7 mm at U_{in}=0.41 m/s, whereas the both minimum ones are 1 mm at the neighborhood of transition velocity ($U_{in} = 1.04$ m/s), as shown in Table 4.2 and 4.3. Comparing with $\alpha=100\%$, the difference in maximum flame thickness is 0.7mm at the same incoming airflow

velocity 0.41 m/s, the reasons are the same as mentioned in Chapter 4.3.1.1. The differences in flame thickness between α=100% and α=60% are 0.3mm at both critical U_{in} = 1.24m/s and 1.04 m/s. This may indicate that the stretch effect is more apparent for the flame with a lower methane to nitrogen mass ratio. For the comparison of stand-off distance, the trend is similar to that α=80% with α=100%, referred in Chapter 4.3.1.1. When α is below 60%, the measurement of temperature by inserting the probe into the envelop flame front causes it blown off in the front of cylinder burner, indicating that the flame in this regime is quite weak and it cannot sustain with the quenching effect of the thermocouple junction. Therefore, in this experiment the envelope flame temperature distributions in the front of the cylinder burner are not measured at 60%, 50% and 40%.

Figure 4.13 shows the seven temperature measurements downstream of the burner as a function incoming flow velocity. The trend for the temperature variation at these measuring positions of α=60% is similar to that of α=100%, as expected, the temperatures for α=60% is lower.

4.3.2.2 Wake Flame

At α=60%, the flame front can stabilize on the rear surface of the cylinder as shown in Figs. 4.12(c) and 4.12(d) when the inflow velocity exceeds 1.06 m/sec. At U_{in}= 1.06 m/s, the wake flame transition limit velocity, its attached angle is 152°(see Table 4.4). Comparing the variation of attached angle as a function of U_{in} with α=100%, the trend is similar. The attached angle of α=100% is slight higher than that of α=60% at the same velocity. For example, at U_{in}= 1.77 m/s, it is at 141° for α=100%, and 135° for α=60%.

The temperature distributions in the rear of the cylinder burner are shown in the Fig. 4.13.   The temperatures at the present case are slightly lower than those at α=100%, the reasons are the same as mentioned in Chapter 4.3.1.3.   As U_{in} gradually increase up to 1.87 m/s, the general trend of temperature variation is similar to that of α=100%, but the temperatures at 45mm and 60mm of measuring position are found lower than the one at 30 mm as U_{in} is below 1.48m/s.   It is because that the combustion plume becomes smaller comparing to that of α=100% as methane to nitrogen ratio decreases.   Furthermore, as U_{in} is greater than 1.87 m/s, the temperature trend is decreasing due to the termination of combustion plume.

4.4 Comparisons with Chen's Numerical Simulation [14]

A colleague, Chen [14], modifies the two-dimensional combustion model developed previously by Chen and Weng [1] by using an energy balance to treat the temperature on the surface over a Tsuji burner instead of the assumption that temperature is fixed (400K). The present experimental results are compared with his corresponding predictions to verify the validity of the numerical combustion model, and to intensify the interpolation on the physical mechanisms. The compared objects are the flame transitional trend, the envelop flame stand-off distance and thickness as well as the attached angle of stable wake flame.

4.4.1 Flame Transition Trend

Figure 4.15 depicts the resultant flame structures as functions of U_{in}, and Y_{CH_4} by the present experimental work and Chen's numerical

simulation. In this figure, both the experimental observed values (dash line) and numerical predictions (solid line) are plotted together and they are found to have the same qualitative trend. From the quantitative point of view, it can be found that the transition gap between envelop and wake flame does not exist when Y_{CH_4} is less than 0.6 for both experiment and simulation. In other words, the envelop flame is directly transformed into wake one as the critical velocity is reached in that regime. However, the transition velocities from envelop to wake flames, envelop to transition flames and transition to stable wake flames obtained from experiments appear to be higher than predictions. The major reason for this discrepancy may mainly attribute to the preheating effect of incoming flow, which let flame become stronger, in experiment mentioned previously, although the numerical model adopts the one-step overall chemical kinetics. Of course, the uncertainty of velocity provided by blower and three-dimensional effect may also contribute to the discrepancy. Also, the predicted transition region, existed as the methane mass fraction (Y_{CH_4}) greater than 0.6, has a smaller gap than the one measured experimentally. This main reason may attribute to that this study cannot take more meticulous measurements due to the fixed but not continuous graduation in the control of blower frequency. In other words, the transition velocity in experiment may be over specified.

As mentioned previously, in the higher methane mass fraction regime, ($Y_{CH_4} > 0.6$), a transition zone existing between envelop and wake flame regimes is identified. In such zone, the flame is highly unstable

and it may be lift-off flame, wake flame or extinction. Whenever the lift-off flame appears, it can only sustain for 5~8 seconds, and then it disappears. However, it either shows a stable lift-off flame or becomes extinction by a slight increment of inflow velocity in Chen's numerical simulation [14].   By comparing numerical predictions with experimental observations, it can show that Chen's combustion model can well predict the flame transition limits and present the envelope and wake flame configurations. However, for the lift-off flame, this model can only offer the corresponding flame structure simulation and phenomenon analyses. Therefore, this experimental study suggests that Chen develop a transient program to investigate them further.

4.4.2 Stand-off distance and Thickness of Envelop Flame

It has been mentioned that the experiment adopts blue flame boundary obtained from spotlight software (Chapter 2.4.3) to determinate the flame boundary. However, in Chen's simulations, he adopts the contour line of $\bar{\dot{\omega}}_{CH_4} = 10^{-4} \frac{g}{cm^3 \cdot \sec}$ in the mass fraction distribution as the flame boundary.

Table 4.3 and Table 4.6 summarize the data of the flame stand-off distance at various inflow velocity (U_{in}) and methane/nitrogen mass ratio (α) from for the experimental observed values and numerical predictions, respectively. Table 4.2 and Table 4.5 summarize the data of flame thickness.

The experimental data in Table 4.3 show that for a fixed α, the flame stand-off distance declines in a stepwise trend as U_{in} increases. On the

other hand, for a fixed U_{in}, the flame stand-off distance is almost invariant as α decreases. However, in Chen's simulations as shown in Table 4.6, the flame distance declines gradually as inflow velocity increases or methane mass fraction decreases. The reason may attribute to that this experiment cannot identify the slight displacement discrepancy due to the pixel and resolution in photographs as discussed in Chapter 2.4.3. Besides, from the Table 4.3 and Table 4.6, it can be found that the flame stand-off distances obtained from experiments appear to be shorter than the ones from predictions. It may mainly attribute to the assumption that the buoyancy effect is not under consideration in Chen's combustion model.

This experimental data in Table 4.2 show that under a fixed α, the flame thickness becomes thinner with a manner of step-wise variation as the inflow velocity increases. So do in Chen's simulations, but the variation is continuous as shown in Table 4.5. The main reason may attribute to the insufficiency in pixel and resolution of experimental photographs, as mentioned previously. Also, from the comparison between Table 4.2 and Table 4.5, it finds the flame thickness obtained from experiments appear to be smaller than predictions. This reason may attribute to the different determination methods of the flame boundary in experimental observations and predictions, as mentioned previously. Of course, the simulation is two dimensional, whereas the experiment is three dimensional. From Chen's numerical simulation, it finds that increasing the incoming flow velocity enhances the flame stretch effect. However, the flame stretch effect increases gradually along the cylinder surface and it's influence is very slight, as shown in Table 4.5

4.4.3 Wake Flame Attached Angle

Table 4.4 and Table 4.7 summarize the data for wake flame attached angle at various inflow velocity and methane mass fraction for experimental observed values and numerical predictions, respectively.

This experimental data in Table 4.4 show that the initial attached angles are almost invariant, $\theta \cong 150^0$, when the flame begins to become a stable wake flame for various methane mass fractions. As the inflow velocity increases, the attached angle become smaller gradually and it reaches a critical value eventually. The critical attached angle is about $\theta \cong 120^0$. However, from Chen's predicted data listed in Table 4.7, it finds that at the higher methane mass fraction regime ($Y_{CH_4} \geq 0.6$), the initial attached angles are $\theta \cong 135^0$ when the flame begins to become a stable wake flame, and they will become smaller and reaches $\theta \cong 120^0$ eventually. The trend that attached angle becomes smaller with an increase of the inflow velocity is qualitatively similar for both experiment and simulation. However, it is larger experimentally. This discrepancy may mainly attribute to the assumption that the overall one-step chemical kinetics is adopted in Chen's numerical combustion model, which leads to a stronger combustion. Of course, the consideration without the thermal buoyant effect also contributes to the discrepancy. On the other hand, at the lower methane mass fraction ($Y_{CH_4} < 0.6$), the variation for the attached angle of wake flame is irregular and it is near $\theta \cong 120^0$. This main reason may attribute to the assumption that overall one-step chemical kinetics is adopted in Chen's numerical combustion model, as

mentioned above. Therefore, this experiment suggests that Chen's numerical combustion model adopt four-step chemical kinetics to simulate the stable wake flame if he wishes to obtain more exact quantitative dada about the attached angle, especial at lower methane mass fraction.

4.5 Comparisons with Chang's Experiments [1]

In Chang's experiment, it investigates flame lift-off phenomenon over a cylinder burner. Its variation parameters were the incoming airflow velocity, U_{in}, and the fuel ejection velocity, V_w, respectively. The fuel used was pure methane, ejecting from the forward half part of the burn at blowing velocity, V_w=0.9~3.02 cm/s. He found that in the regime of $V_W < 0.0291$ m/s, the envelope flame will transform into wake one directly when incoming velocity gradually increases to a limiting value. On the other hand, in the regime of $V_W \geq 0.0291$ m/s., the flame structures will appear three types, envelope, wake, and lift-off flames when incoming airflow velocity, U_{in}, increases. The lift-off flame phenomenon is also found in this study under a fixed blowing velocity, $V_w = 0.05$m/s for pure methane fuel. In addition, this study also finds that for methane/nitrogen fuel ejected from the forward half part with $V_w = 0.05$m/s, in the lower methane mass fraction regime, ($Y_{CH_4} \leq 0.6$), the enveloped flame is directly transformed into wake one as the transition velocity is reached. On the other hand, in the higher methane mass fraction regime, ($Y_{CH_4} > 0.6$), the lift-off flame is found between envelop

and wake flame when incoming velocity gradually increases.   However, It shows oscillatory feature and can only sustain for less than 8 sec, then disappears. Comparing with Chang's experiment, this study finds that the critical value and the methane mass blowing rate (ρ_{CH_4} Q, where ρ_{CH_4} is the density of methane and Q is volume rate) that lift-off flame occurs, are nearly the same for both experimental studies. Although, the measured value in this study is slightly higher than the one in Chang's experiment. However, this discrepancy is in the error range of mass flow controller. In addition, the lift-off flame always occurs at higher methane mass blowing rate. Hence, this study believes that lift-off flame is an unstable phenomenon caused by too much methane mass supply when transition velocity, where the enveloped flame is transformed into wake one, is reached.

CHAPTER 5
CONCLUSIONS

The flame transition processes over a single Tsuji burner as the functions of methane to nitrogen mass ratio (α) and incoming air flow velocity (U_{in}) under a fixed blowing velocity (V_w=0.05m/s) was investigated in this thesis. The corresponding measurements of temperature distributions along the vertical centerline also were carried out. The basic experimental apparatuses in the present study are the same as those of Chang's [1]. The major improvements include that a gas mixer is employed to generate the assigned fuel mixture of nitrogen/methane and an instrumentation in test section is adopted to measure the flame temperature distributions mentioned above.

From the experimental observation, it finds that the transition velocity is reduced as the mass fraction of methane in fuel mixture is lowered because the flame becomes weaker. In the higher methane mass fraction regime, ($\alpha > 60\%$), the envelop, transition and wake flames appear in order as the incoming flow velocity increases from 0.41 to 2.63 m/sec. A transition zone between envelop and wake flame regions is identified in this regime. In such zone, the flame shows an oscillatory feature and can be survived only for 5~8 seconds. It is highly unstable that it might appear as a lift-off flame, wake flame or extinction. On the other hand, when the methane to nitrogen mass ratio is below 60% ($\alpha \leq 60\%$), the envelope flame is directly transformed into wake one as incoming velocity gradually increases up to the transition velocity, and no

transition flame is identified in this regime.

In the envelope flame regime, an increase of incoming flow velocity represents an increase in flame stretch so that the flame thickness becomes thinner. As methane to nitrogen mass ratio decreases from 100% to 40%, the flame thickness is decreases. In the meantime, the convection of air flow becomes stronger to push flame front toward the burner surface that the stand-off distance is lowered.   However, it strongly depends on the incoming airflow velocity, but not so strongly on the methane to nitrogen mass ratio. In the envelope flame temperature ahead of the burner, the temperature at the same position decreases as the flow velocity increases. On the other hand, the envelope temperature behind of the burner at the same position increases as the flow velocity increases. Under the same incoming flow velocity, the envelope flame temperature decreases as the methane to nitrogen mass ratio decreases.

In the wake flame regime, as incoming airflow velocity increases, the wake flame attached angle is decreased under the same methane to nitrogen mass ratio. Under the same incoming airflow velocity, the attached angle is slight decreased with a decrease of methane to nitrogen mass ratio. The wake flame temperatures behind a cylindrical burner at $\alpha = 100\%$ (pure methane fuel) gradually increase at the beginning, then, increase very slightly as inflow velocity increases from $U_{in} = 2.06$ to 2.63 m/s. At $\alpha = 80\%$ and $\alpha = 60\%$, the temperatures do not increase gradually with an increase of inflow velocity as the inflow velocity increases to a critical value.   After that, the temperatures decrease.

A comparison is made with Chen's [14] predictions for the characteristics of various flame structures and transitional trend. The

envelope flame thickness and stand-off distance obtained from experiments appear to be smaller than those from predictions. It may mainly attribute to the assumption that the buoyancy effect is not under consideration in Chen's combustion model and the different determination methods of the flame boundary in experimental observations and predictions. The wake flame attached angles obtained from experiments are higher than the corresponding ones from predictions. This discrepancy may mainly attribute to the overall one-step chemical kinetics assumption adopted by Chen's numerical combustion model. As to the transition velocities, they are higher in experiments because the preheating effect of incoming flow in the experiment is inevitable and the three-dimensional effect may also contribute to the discrepancy.

Finally, several modifications are suggested for further modification of the present experiment. The particle image velocimetry (PIV) incorporates with a LASER system to generate a picture for the moving magnesium oxide particles ejected into the uniform air stream to analyze the flow pattern and flow velocity in various flame structures. The flame temperature distribution is measured by Schlieren system that can further explain the flame structure. Furthermore, to investigate the duality and hysteresis phenomena by varying the incoming airflow velocity from a higher one to lower one under different methane to nitrogen mass is also proposed.

References

1. C. C. Chang, Experimental Visualization of Counterflow Diffusion Flame over a Porous Cylinder, M. S. thesis, National Chiao Tung University, Taiwan, 2002.

2. C. H. Chen and S. S. Tsa, Flame stabilization over a Tsuji burner by four-step chemical reaction, *Combustion Science and Technology*, vol. 175, pp.2061-2093

3. C. H. Chen and F. B. Weng, Flame Stabilization and Blowoff Over a Porous Cylinder, *Combustion Science and Technology*, vol. 73, pp. 427-446, 1990.

4. H. Z. Chen, Experimental Visualization for Flows over the Porous Spheres and Cylinder with/without Blowing, M. S. thesis, National Chiao Tung University, Taiwan, 2004.

5. H. Tsuji and I. Yamaoka, The Counterflow Diffusion Flame in the Forward Stagnation Region of a Porous Cylinder, *Eleventh Symposium (International) on Combustion*, pp. 979-984, 1967.

6. H. Tsuji, and I. Yamaoka, The Structure of Counterflow Diffusion Flame in the Stagnation Region of a Porous Cylinder, *Twelfth Symposium (International) on Combustion*, pp. 997-1005, 1969.

7. H. Tsuji and I. Yamaoka, Structure Analysis of Counterflow Diffusion Flames in the Forward Region of a Porous Cylinder, *Thirteenth Symposium (International) on Combustion*, pp. 723-731, 1971.

8. H. Tsuji and I. Yamaoka, Structure Analysis of Anomalous behavior of methane-air and methane-hydrogen-air flames diluted with nitrogen in a stagnation flow, *Thirteenth Symposium (International) on Combustion*, pp. 145-152, 1992.

9. H. Tsuji and S. Ishizuka, An Experimental Study of Effect of Inert Gas on Extinction of Lamina Diffusion Flames, *Eighteenth Symposium (International) on Combustion*, pp. 695-703, 1981

10. R. Dirk, F. Toshiro and S. Jun'ichi, Effect of dilution on extinction of methane diffusion flame in high temperature air up to 1500 K, *Combustion Science and Technology*, vol. 174, pp. 23-46, 2002.

11. T. L. Jiang, W. S. Chen, M. J. Tsai and H. H. Chiu, Double Flame and Multiple Solution Computer for a Wetted Porous Sphere Vaporizing in Reactive Flows, *Combustion Science and Technology*, vol. 102, pp. 115-143, 1994.

12. A. Makino, N. Araki and Y. Nitta, The Structure of

Partially-Premixed Diffusion Flame (Investigation of the Flame Structure Near the Blow-Off Limit with CARS), 日本機械學會論文集(B編)57卷553號,1991.

13. S. R. Gollahalli and A. T. Brzustowski, Experimental studies on the Flame Structure in the Wake of a Burning Droplet, *Fourteenth Symposium (International) on Combustion*, pp.1333-1344, 1973

14. D. D. Chen, The Numerical Analyses of Flame Behaviors and Blow-off limit over a Tsuji Burner for Methane/Nitrogen and Methane/Air Fuels, Ph. D. Dissertation, National Chiao Tung University, Taiwan, 2005.

15. J. C. Yang, M. K. Donnelly, N. C. Prive, and W. L. Grosshandler, Dispersed Liquid Agent Fire Suppression Screen Apparatus, NISTIR 6319, *National Institute of Standards and Technology*, 1999.

16. Laboratory Methods of Testing Fans for Rating, ANSI/AMCA 210-85 Standard, 1985.

17. V. R. Chen, Experimental Visualization and Measurements for Flame Interaction Between Dual Tsuji Burners in Side-by-Side Arrangement, M. S. thesis, National Chiao Tung University, Taiwan, 2003.

18. R. W. Fox, and A. T. McDonald, Introduction to Fluid Mechanics, John Wiley and Sons, Canada, 1994.

19. S. J. Kline, and F. Mcclintock, Describing Uncertainties in Single-Sample Experiments, *Mechanical Engineering*, vol. 75, pp. 3-8, 1953.

20. R. J. Moffat, Contributions to the Theory of Single-Sample Uncertainty Analysis, *Journal of Fluid Engineering*, vol. 104, pp. 250-260, 1982.

21. R. S. Figliola, and D. E. Beasley, Theory and Design for Mechanical Measurements, 2nd Ed., John Wiley and Sons, Canada, 1995.

22. J. P. Holman, *Experimental Methods for Engineers*, 5th Ed., McGraw-Hill, New York, 1989.

23. D. Bradley and K. J. Matthews, Measurement of High Gas Temperatures with Fine Wire Thermocouples, *Journal of Mechanical Engineering Science*, vol. 10, No. 4, pp. 299-305, 1968.